Medical Image Segmentation using Object Atlas versus Object Cloud Models

Renzo Phellan[a], Alexandre X. Falcão[a], Jayaram K. Udupa[b]

[a]LIV, Institute of Computing, University of Campinas, Campinas, SP, Brazil;
[b]MIPG, Dept. of Radiology, University of Pennsylvania, Philadelphia, PA, USA

ABSTRACT

Medical image segmentation is crucial for quantitative organ analysis and surgical planning. Since interactive segmentation is not practical in a production-mode clinical setting, automatic methods based on 3D object appearance models have been proposed. Among them, approaches based on object atlas are the most actively investigated. A key drawback of these approaches is that they require a time-costly image registration process to build and deploy the atlas. Object cloud models (OCM) have been introduced to avoid registration, considerably speeding up the whole process, but they have not been compared to object atlas models (OAM). The present paper fills this gap by presenting a comparative analysis of the two approaches in the task of individually segmenting nine anatomical structures of the human body. Our results indicate that OCM achieve a statistically significant better accuracy for seven anatomical structures, in terms of Dice Similarity Coefficient and Average Symmetric Surface Distance.

Keywords: Object fuzzy models, probabilistic atlas, object appearance models, 3D medical image segmentation

1. INTRODUCTION

Quantitative organ analysis and surgical planning often require a precise segmentation of the organs and other anatomical structures contained in 3D medical images of the patient.[1] This task can be done interactively/manually by medical experts. However, manual segmentation is a time-consuming, tedious and error-prone task, subject to intra- and inter-observer variability.[2] In order to solve this problem, automatic segmentation methods based on object appearance models have been proposed. These approaches build a statistical/fuzzy model from a set of training images and their respective object masks, as obtained by interactive segmentation. The model is then used to detect and delineate the object in each new image.

Object atlas models (OAM)[2–4] are the most popular ones. The model appears as a probabilistic object, with a very narrow uncertainty region. By thresholding the probability values, one can obtain objects with the 3D shape of the anatomical structure. OAM construction requires the selection of a training image to be the reference coordinate system and the time-costly registration of the other training images into that system. The 3D anatomical structure in a new image is detected by also registering the image into the atlas coordinate system, which usually takes some minutes. Object delineation can then be simplified, for instance, to voxel classification.[2] Object cloud models (OCM)[5] avoid registration by building the model simply based on translations of the training masks to a common reference point (their object centers). As a result, the model presents a fuzzy appearance of the object's shape, with an uncertainty region larger than the one of OAM due to the abscence of registration. Object detection in a new image requires to translate the model over the image, delineate a candidate object at each position within the uncertainty region of the model, and evaluate each delineation score, which should be maximum at the correct anatomical structure's position. Such a simplification with a clever implementation of the object search process allows to complete segmentation in some seconds per anatomical structure. Moreover, model construction also takes some seconds per object rather than hours, as in OAMs.

Further author information:
Renzo Phellan: E-mail: ra144686@students.ic.unicamp.br
Alexandre X. Falcão: E-mail: afalcao@ic.unicamp.br
Jayaram K. Udupa: E-mail: jay@mail.med.upenn.edu

Medical Imaging 2015: Image-Guided Procedures, Robotic Interventions, and Modeling,
edited by Ziv R. Yaniv, Robert J. Webster III, Proc. of SPIE Vol. 9415, 94151M

Contributions The advantages in computational time of OCM over OAM makes the former more attactive, but it is also important to compare their accuracies in segmentation. The present work fills up this gap. We detail our implementation of each model, OAM and OCM, and discuss the situations where one approach has advantages over the other. Besides, for OCM, we propose a combined image gradient which considers not only the local properties of the image, but also the information about the anatomical structures range of gray values, which is learnt from the training set. We also sped up the OCM usage phase by constraining the search process of the anatomical structure to a reduced region that is learnt during the training phase and optimizing it using the MSPS algorithm.

1.1 Related work

Image segmentation methods can be divided into object-model-based, image-based, and hybrid approaches.[6] Object-model-based methods create a statistical/fuzzy model for the appearance (shape and/or texture) of the objects. Active Shape Models[7,8] and Object Atlas Models (OAM)[2–4] are well known approaches, being the latter more actively pursued in medical image segmentation. OAM is robust to noise and can preserve the object's shape even in the absence of boundary contrast,[2] but it can lead to errors due to imperfect registration of a new image and the lack of flexibility in locally fine tuning the object's boundary.[9] On the other hand, image-based methods[6,10–14] take into account local image properties to delineate the object as it actually appears in the new image. Although they can better adapt to the local shape features of the anatomical structures, they may not preserve their global shape.[9] As a result, image-based methods have been usually used for interactive segmentation, performing object delineation from user-drawn markers.

Hybrid approaches[1,2,5,9,15–18] aim to combine the strengths from both, image-based and object-model-based methods, to improve automatic segmentation. The basic idea is to use the shape model to locate the object in a new image and guide its delineation by image-based methods.

In hybrid approaches based on OAM, the choice of the atlas coordinate system is very important to avoid segmentation bias towards the reference mask.[19] However, the main drawback in OAM approaches[2,9,16,17] is the need for affine followed by locally deformable registration to map the training images onto the atlas coordinate system. This process can take hours per anatomical structure, depending on the training set size. Moreover, the registration of the new image into the atlas coordinate system also takes some minutes.

When using a software tool for medical image analysis, the expert usually has to interact with the software and does not usually want to wait that long, especially if the number of images for analysis is high. In this sense, approaches that avoid image registration are more attractive. The resulting fuzzy object model, however, presents a larger uncertainty region, requiring a more accurate image-based approach for delineation. The object cloud models (OCM)[5,15] are built based only on training mask translations, but their rotation to align each training object with its principal axes has also been proposed in order to reduce the uncertainty region of the model.[1,18]

In this paper, we compare OCM and OAM for the case of single-object segmentation. Both approaches have been extended to multi-object segmentation[1,15,18,20–23] and their comparison in this context will be a future work.

2. SEGMENTATION USING OBJECT ATLAS MODEL

In this section we give the technical details to construct an object atlas model (OAM) and use it to segment a new image. In order to avoid segmentation bias toward the reference mask,[19] we computed the distances between each pair of training mask and selected the one whose average distance to the others is minimum. We used the Average Symmetric Surface Distance (ASSD)[24] for this task, because it can better detect the local differences between boundaries than global measures, such as Dice Similarity Coefficient (DSC), for instance. In order to allow locally fine tuning to the object's boundary,[9] segmentation is based on the posterior probability values as estimated for each new image. That is, the object is delineated by thresholding the posterior probability map at value 0.5.

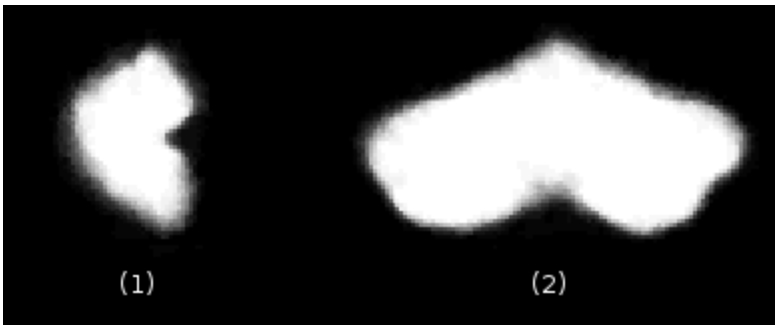

Figure 1. Prior probability map of the cerebellum: (1) sagittal slice and (2) coronal slice.

2.1 Atlas construction

For a given anatomical structure of interest O and training set of medical images with their respective object masks, we select the atlas reference system as described above and register all training masks into that system with affine transformation followed by locally deformable image transformation.

Image registration was computed by the software tool described in[25] publicly available at http://elastix.isi.uu.nl. Its parameters were configured as suggested in.[16] The affine transformation in this tool is rigid and the locally deformable transformation is based on B-splines. Both use mutual information as optimality measure for registration. The resulting deformation field for the original image is then applied to transform its respective binary mask.

In the atlas coordinate system, the training masks are averaged to compute a prior probability map (i.e., the atlas). This process can be formalized as follows.

Definition 2.1 (Medical image). *A medical image $\hat{I}$ is a pair (D_I, I) where $D_I \in Z^3$ is the image domain and $I(v) \in Z$ is a scalar value assigned to every voxel $v \in D_I$. Image $\hat{I}$ is said* binary*, when $I(v) \in \{0, 1\}$.*

Definition 2.2 (Prior probability Map). *In the atlas reference system, the prior probability $P(v \in O)$ of a voxel v to belong to an anatomical structure O is measured as the percentage of times that $I(v) = 1$ at location v in the training binary masks.*

2.2 Segmentation with the atlas

For a given new image containing the anatomical structure O, we must first register it into the atlas coordinate system. The anatomical structure could be segmented by thresholding the atlas at 0.5, but this would disregard the local image properties of the anatomical structure in the new image. We take into account these properties by estimating the conditional probability density, the joint probability density, and finally the posterior probability map, as follows.

Definition 2.3 (Conditional probability density). *Let $x = I(v)$ be a random variable. In our case, the conditional probability density $\rho(x \backslash v \in O)$ is a Gaussian distribution, whose mean and standard deviation are computed over the intensities of the voxels in O, using all training images.*

Definition 2.4 (Posterior probability). *By Bayes's formula, the posterior probability is*

$$P(v \in O \backslash x) \quad = \quad \frac{P(v \in O)\rho(x \backslash v \in O)}{\rho(x)}, \tag{1}$$

where the joint probability density $\rho(x)$ is simply the normalized histogram of the new image.

The anatomical structure is then segmented by selecting voxels v such that $P(v \in O \backslash x) \geq 0.5$. Figures 1, 2 and 3 illustrate the resulting images that represent the prior probability map (atlas), conditional probability density map, and posterior probability map in the atlas coordinate system of the cerebellum, as obtained from MR-T1 images.

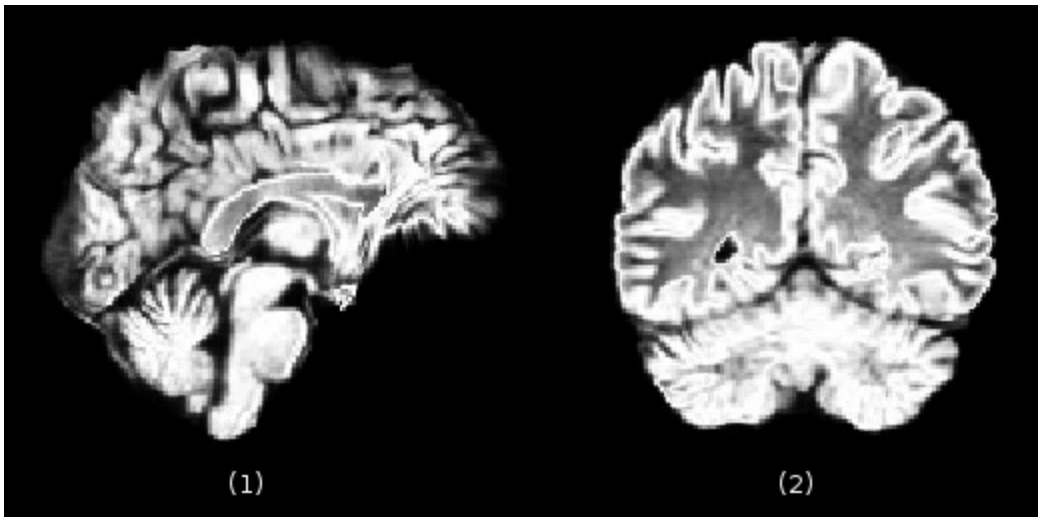

Figure 2. Conditional probability density map of the cerebellum: (1) sagittal slice (2) coronal slice.

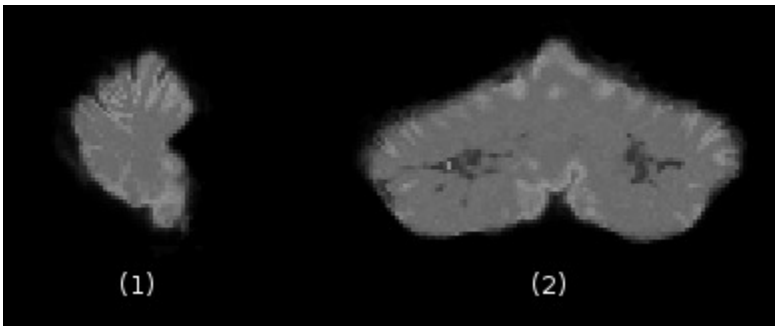

Figure 3. Posterior probability map for a new image of the cerebellum: (1) sagittal slice (2) coronal slice.

3. SEGMENTATION USING OBJECT CLOUD MODEL

An object cloud model (OCM) for a given anatomical structure O can be formally defined as follows.

DEFINITION 3.1 (OBJECT CLOUD MODEL). *An object cloud model is a triple that consists of a fuzzy object $\hat{O}_f$, a delineation algorithm A and a functional F.*[5]

The fuzzy object $\hat{O}_f$ is obtained by translating all training masks to a same reference point (the geometric center of their objects) and averaging their values. For a given new image, the fuzzy object $\hat{O}_f$ translates over the image and, for each position, algorithm A is executed inside the uncertainty region of $\hat{O}_f$ to obtain a candidate segmentation. The functional F is evaluated on this segmentation to obtain a matching score, by taking into account local and global object properties. The desired segmentation is expected to be the one with maximum score.

The object search process can be optimized by several ways. In,[5] the authors execute exhaustive search in three scales of image resolution in order to speed up the process. We optimized this process by estimating the search region (a small fraction of the image) from the translations of the training masks during the model's construction and applying an optimization algorithm.[26]

3.1 Fuzzy object construction

The fuzzy object of the cloud model can be defined as follows.

DEFINITION 3.2 (FUZZY OBJECT). *A fuzzy object $\hat{O}_f = (D_{O_f}, O_f)$ is an image created by translating the geometric centers of the objects in all training masks to the center of the image domain $D_{O_f} \in Z^3$ and averaging*

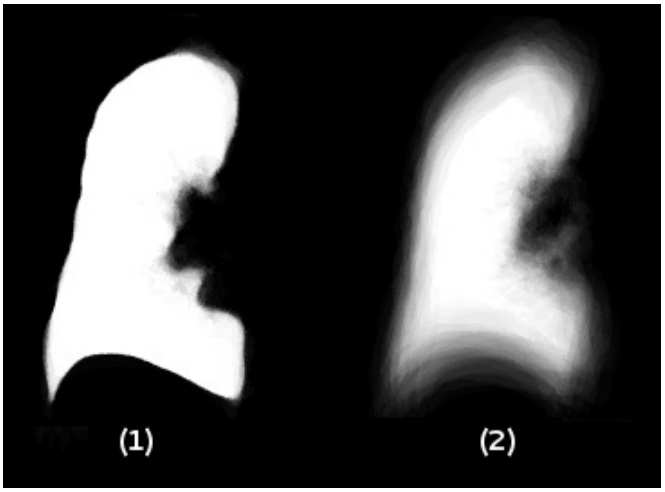

Figure 4. Coronal slices of the object (1) atlas and (2) cloud models of the right pleural sac.

their binary intensities $I(v) \in \{0,1\}$ *for each voxel* $v \in D_{O_f}$. D_{O_f} must be big enough to accomodate all training objects in it.

Figure 4 shows both, the probabilistic atlas and the fuzzy object of the right pleural sac, as obtained from CT images of the thorax. Due to the absence of registration and also motion of the lungs, the uncertainty region of the fuzzy object tends to be much larger. The uncertainty region $\mathcal{U}$ is defined by voxels $v \in D_{O_f}$ such that $O_f(v) \in (0,1)$. The interior $O_f(v) = 1$ and exterior $O_f(v) = 0$ are defined by voxels that are either inside or outside of any training mask, respectively. Such a wider uncertainty region requires higher effectiveness of the delineation algorithm A than the one used in OAM to locally fine tuning the object's boundary.

3.2 Delineation algorithm

For delineation, we have selected the image foresting transform (IFT) algorithm from seed competition,[13] as suggested in.[5] It interprets an image $\hat{I}$ as a graph $(D_I, \mathcal{A})$ by taking an adjacency relation $\mathcal{A} \subset D_I \times D_I$ between voxels. For segmentation, we use $\mathcal{A}$ as a 26-neighborhood where a voxel v' belongs to the adjacent set $\mathcal{A}(v)$ of a voxel v when $\|v' - v\| \leq \sqrt{3}$. The weight $w(v,v')$ of each arc in $\mathcal{A}$ is given by a combination between local image and global object properties.

$$w(v,v') \quad = \quad \alpha G_i(v') + (1-\alpha) G_o(v'), \tag{2}$$

where $G_i(v')$ is the magnitude of the 3D Sobel's gradient of the original image $\hat{I}$ and $G_o(v')$ is the magnitude of the 3D Sobel's gradient of the conditional probability density map $\rho(x \backslash v \in O)$ estimated for image $\hat{I}$ based on its values and the Gaussian distribution learned by training (the same used for the atlas).

Note that, we do not need the segmentation of $\hat{I}$ to estimate its $\rho(x \backslash v \in O)$. Given that $G_o(v')$ may not be perfect, we observed that the best solution is to combine it with $G_i(v')$. The parameter $0 \leq \alpha \leq 1$ is then found by 2-fold cross validation among the training images.

The arc weights are meant to be higher on the object's border than inside and outside it. At any given position of the fuzzy object $\hat{O}_f$ in the image, the interior and exterior voxels are used to define seed sets $\mathcal{S}_i$ and $\mathcal{S}_e$, which must compete for the most closely connected voxels in $\mathcal{U}$, as in.[5] This competition then considers a reduced graph $(D_U, \mathcal{A})$, where $D_U = \mathcal{U} \cup \mathcal{S}_i \cup \mathcal{S}_e$ and a path-cost function $f(\pi_v)$ applied to any path $\pi_v = \langle v_1, v_2, \ldots, v_n \rangle$, $v_n = v$, in the graph, including the trivial ones $\langle v \rangle$ formed by a single voxel.

$$\begin{aligned} f(\langle v \rangle) \quad &= \quad \begin{cases} 0 & \text{if } v \in \mathcal{S}_i \cup \mathcal{S}_e, \\ +\infty & \text{otherwise,} \end{cases} \\ f(\langle v_1, v_2, \ldots, v_n \rangle) \quad &= \quad \max_{i=1,2,\ldots,n-1} \{ w(v_i, v_{i+1}) \}. \end{aligned} \tag{3}$$

Figure 5. Sets $\mathcal{S}_i$ (red) and $\mathcal{S}_e$ (yellow) for right pleural sac: (1) axial slice (2) coronal slice.

The IFT algorithm then minimizes a cost map

$$C(v) = \min_{\forall \pi_v \in \Pi(D_U, \mathcal{A}, v)} \{f(\pi_v)\} \quad (4)$$

by computing an optimum-path forest rooted at $\mathcal{S}_i \cup \mathcal{S}_e$. That is, considering the set $\Pi(D_U, \mathcal{A}, v)$ of all possible paths π_v from $\mathcal{S}_i \cup \mathcal{S}_e$ to every voxel $v \in D_U$, the algorithm assigns to v the path π_v^* of minimum cost, such that the object is defined by the union between the interior voxels and the voxels of $\mathcal{U}$ that are rooted in $\mathcal{S}_i$.

This seed competition process avoids paths that cross the object's border as much as possible due to the design of the path-cost function and minimization of the cost map. The operator can also be sought as an improved watershed transform from internal and external markers, but with gradient formulation, markers, and delineation algorithm different from the one proposed in.[17] Figure 5 shows the sets $\mathcal{S}_i$ and $\mathcal{S}_e$ for the right pleural sac.

3.3 Criterion function

For the functional F, which scores the candidates O, we chose the mean arc weight along the IFT graph cut, as suggested in.[5]

$$score(O) = \frac{1}{|B_O|} \sum_{\forall (v,v') \in B_O} w(v, v') \quad (5)$$

where $B_O : (v, v') \in \mathcal{A} \backslash v \in O, v' \notin O$.

3.4 Optimized search algorithm

As we mentioned, the fuzzy object $\hat{O}_f$ translates over the image, seeking for a maximum score. However, instead of using exhaustive search, we speed up the search process by constraining the Multi Scale Parameter Search (MSPS) optimization algorithm[26] in a region around the center of D_{O_f}. This region is learned from the training set by recording the relative positions between the geometric centers of the object masks and the center of D_{O_f}. An alternative method for the case of brain images, for instance, is to previously align images by their Midsagittal Plane and then apply multi-resolution search refinement, as presented in.[20]

The MSPS algorithm further speeds up the search for the best candidate by avoiding delineation in all points of the search region in order to obtain the solution as the candidate O with maximum $score(O)$. The parameters

Anat. Str.	Alpha (α)	Image Vol. (voxels)	SR Vol. (voxels)	SR (%)
C	0.5	6 912 015	1 656	0.0240
LH	0.2	6 912 015	100	0.0014
RH	0.1	6 912 015	125	0.0018
TSkn	0.2	16 252 928	5 148	0.0317
LPS	0.8	16 252 928	30 240	0.1861
RPS	0.8	16 252 928	29 160	0.1794
RS	0.8	16 252 928	20 250	0.1246
IMS	0.4	2 895 824	8 775	0.3030
PC	0.0	2 895 824	13 243	0.4573

Table 1. Values of α and search region.

of this algorithm are the three possible translations along x, y, and z. From an initial position at the center of D_{O_f} and delineation score, the algorithm perturbs the system by displacements along x, y, and z in different scales of the parameter space to avoid local maxima. From the position that holds the maximum score after perturbation, the algorithm repeats the process until no improvement be observed in the score.

By combining the search in different scales, the method performs a broader look at the behavior of the criterion function, which is suitable to deal with the nonconvexity of the problem. The MSPS scales are set according to the bounding constraints inherent to the problem. Three scales $s1$, $s2$ and $s3$ are used for each parameter in this study. They are calculated as a proportion of the dimensions Dx, Dy, Dz of the search region, where $s1_i = MAX(1, 0.1D_i)$, $s2_i = MAX(1, 0.3D_i)$ and $s3_i = MAX(1, 0.5D_i)$, for $i \in x, y, z$. If two scales of a same parameter get a same value, one of them is incremented by 1 until they be different.

4. RESULTS AND DISCUSSION

In this section, we evaluate and compare the models described in sections 2 and 3 (OAM and OCM) using three datasets: (a) 35 MR-T1 images of the brain with voxel size 0.98 x 0.98 x 0.98 mm^3 and their corresponding binary masks for the Cerebellum (C), Left Hemisphere (LH) and Right Hemisphere (RH); (b) 35 CT images of the thorax with voxel size 2.5 x 2.5 x 2.5 mm^3 and their corresponding binary masks for the Internal Mediastinum (IMS) and Pericardial Region (PC); in the case of PC, however, we had only 30 binary masks available; and (c) 40 low-dose CT images of the thorax with voxel size 1.25 x 1.25 x 1.25 mm^3 and their corresponding binary masks for the following anatomical structures: Left Pleural Sac (LPS), Right Pleural Sac (RPS), Respiratory System (RS consisting of LPS, RPS, and trachea and bronchi) and Thoracic Skin (TSkn). Datasets (a) and (b) were segmented by multiple experts using manual and interactive segmentation tools. Dataset (c) was obtained from the VIA/I-ELCAP Public Access Research Database, available at http://www.via.cornell.edu/lungdb.html. It was segmented by using interactive segmentation tools, under the supervision of an expert.

First, Table 4 shows the value of the parameter α for the OCM of each anatomical structure. A previous training phase to tune the parameter α of the combined gradient is required. In order to do that, half of the training set for each anatomical structure was used to tune it, following a Leave-one-out approach. Then, it indicates the total volume in voxels of each image and the volume of the learned search region (SR) mentioned in section 3.3. As we can see, this region represents a very small fraction (less than 1%) of the total volume of the image, so the search process is effectively accelerated, in comparison to a full search.

The experiments randomly divided the datasets 10 times into 70% for training and 30% for test, for statistical analysis. The results were evaluated by two measures: Dice Similarity Coefficient (DSC) and Average Symmetric Surface Distance (ASSD). DSC has been popular in the literature of atlas-based segmentation.[24] However, as pointed out by the authors in,[24] it can over/underestimate the quality of segmentation due to its global characteristic. Therefore, we prefer to draw final conclusions based on ASSD. Anyway, in both cases, we performed a two-tailed Z-test, with a 95% confidence limit. In this case, the critical value for null hypothesis rejection was +/-1.96.

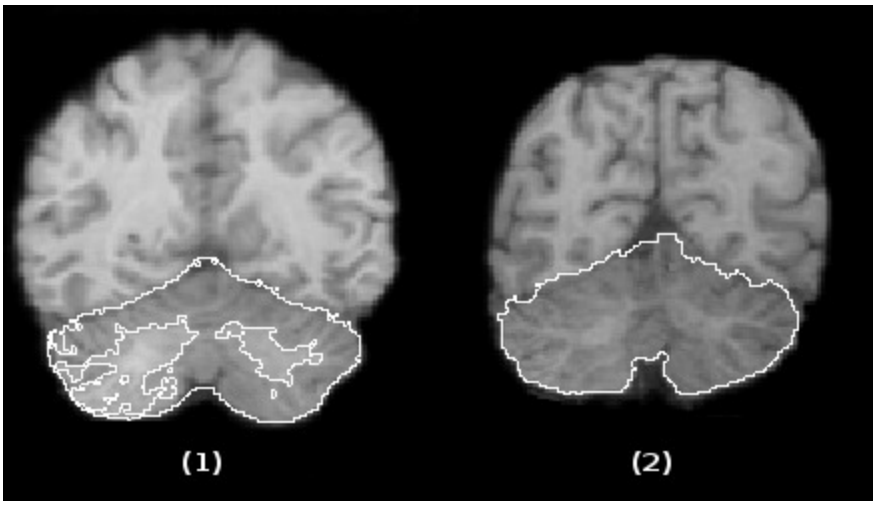

Figure 6. Coronal slice of the cerebellum segmentation using: (1) OAM and (2) OCM.

Anat. Str.	OAM	OCM	Z-score
C	85.28 +/- 2.03	91.28 +/- 0.56	**16.861**
LH	88.69 +/- 5.46	94.29 +/- 0.57	**6.035**
RH	91.50 +/- 3.05	94.94 +/- 0.59	**6.554**
TSkn	86.33 +/- 0.91	98.68 +/- 0.49	**75.828**
LPS	96.39 +/- 0.45	96.72 +/- 0.55	**3.019**
RPS	96.41 +/- 1.84	96.73 +/- 0.79	1.023
RS	97.20 +/- 0.27	97.22 +/- 0.74	0.161
IMS	89.59 +/- 0.49	80.38 +/- 2.70	**-19.846**
PC	86.07 +/- 1.48	86.53 +/- 1.47	1.193

Table 2. DSC accuracies (mean and standard deviation) within [0,100]%. Statistically significant differences are in bold.

4.1 Accuracy

Tables 4.1 and 4.1 show the results for DSC and ASSD, respectively. According to both measures, OCM is better than OAM for 5 out of the 9 anatomical structures (C, LH, RH, TSkn and LPS). However, according to ASSD, OCM is better in 8 cases (C, LH, RH, TSkn, LPS, RPS, RS and PC). This means that OCM produces less pronounced local differences than OAM, thus, it provides better delineation. A segmentation example of the cerebellum can be seen in Figure 6.

The main challenges stem from the abscence of intensity discontinuity on the boundary of the anatomical structure (e.g., IMS) and differences in anatomy among the training objects due to motion of the anatomical structure (e.g. LPS, RPS and RS). Our results suggest that OAM can handle abscence of intensity discontinuity better, because it generates a thinner uncertainty region, so that the segmentation relies more on the model itself than on the delineation algorithm, which requires more defined boundaries. In the cases of anatomical structures with motion, the OCM can successfuly do the segmentation.

4.2 Segmentation time

Table 4.2 shows the times to construct and use the models for a new image. Both using a same computer with an Intel Core i7 processor, at 3.5 GHz, with 32 GB of RAM.

For the OAM segmentation, the construction phase includes choosing a reference image, registering all training images and their binary masks into the atlas reference system, computing the probabilistic atlas, and calculating the parameters of the conditional probability density. The segmentation phase includes registering the new image into the reference space, computing its posterior probability map, and thresholding it at 0.5.

Anat. str.	OAM	OCM	Z-score
C	1.718 +/- 0.215	1.152 +/- 0.074	**-14.748**
LH	2.431 +/- 0.584	1.580 +/- 0.124	**-8.434**
RH	1.533 +/- 0.345	1.308 +/- 0.256	**-3.107**
TSkn	20.538 +/- 0.724	1.616 +/- 0.238	**-157.023**
LPS	4.904 +/- 0.221	2.727 +/- 0.137	**-52.904**
RPS	6.778 +/- 0.370	2.075 +/- 0.263	**-65.577**
RS	5.150 +/- 0.146	2.081 +/- 0.298	**-58.502**
IMS	2.881 +/- 0.122	5.200 +/- 1.043	**13.069**
PC	3.942 +/- 0.326	3.764 +/- 0.324	**-2.120**

Table 3. ASSD (mean and standard deviation) in mm. It is important to notice that, in this case, lesser ASSD means better accuracy. Statistically significant differences are in bold.

Anat. str.	Construction			Use		
	OAM	OCM	Gain	OAM	OCM	Gain
C	9 901.02	5.02	1 972.31	301.31	5.89	51.16
LH	10 202.32	7.71	1 323.26	302.10	8.3	36.40
RH	10 201.40	7.18	1 420.81	301.61	7.24	41.66
TSkn	22 803.84	38.02	599.79	452.91	182.39	2.48
LPS	21 603.95	20.41	1 058.50	453.01	97.43	4.65
RPS	21 603.21	20.66	1 045.65	453.09	95.46	4.75
RS	21 604.09	27.19	794.56	453.00	165.63	2.74
IMS	9 360.35	2.91	3 216.62	360.34	3.79	95.08
PC	8 280.59	1.84	4 500.32	360.24	2.26	159.40

Table 4. OAM and OCM construction and use time in seconds

For the OCM segmentation, the construction phase includes aligning the binary masks, computing the fuzzy object and calculating the conditional probability density. The segmentation phase includes computing both the magnitude of the 3D Sobel's gradient of the original image and the magnitude of the 3D Sobel's gradient of the conditional probability density map. It also includes the optimized search inside the constrained region of the image.

As we can see, OCM represents a considerable improvement in the model construction and use times. This allows the employment of OCM in applications with big sets of medical images. An important observation is that the MSPS algorithm was always able to detect the global maximum in the search region, but this maximum not always corresponded to the correct anatomical structure's position in the image. Therefore, improvements in OCM should be in the model construction, delineation algorithm, and criterion function.

4.3 Future work

Shape variations in the training set due to differences in the size of the anatomical structures, position of the patient and motion may create wide uncertainty regions and cause positioning errors in the seed sets $\mathcal{S}_i$ and $\mathcal{S}_e$ used for delineation when OCM is at the right position in the image. Figure 7 illustrates this situation that will force the IFT algorithm to misdelineate the anatomical structure.

As proposed in ,[20] similar shapes in the training set can be grouped to create multiple OCMs for each anatomical structure or even multiple systems of anatomical structures, with their relative position, for multi-object segmentation, which constitutes what they called Cloud System Models (CSMs). Such a strategy can improve segmentation accuracy using OCMs because it reduces the size of the uncertainty region and avoid mispositioning of seeds. Another possibility is to estimate internal seeds from the skeleton of the OCM's interior region, similarly to the watershed marker selection used in.[17]

We intend to explore the aforemention strategies in future work and also test other delineation algorithms. Some of these ideas, such as grouping and improved delineation, can also be explored in OAM and we intend to verify them as well.

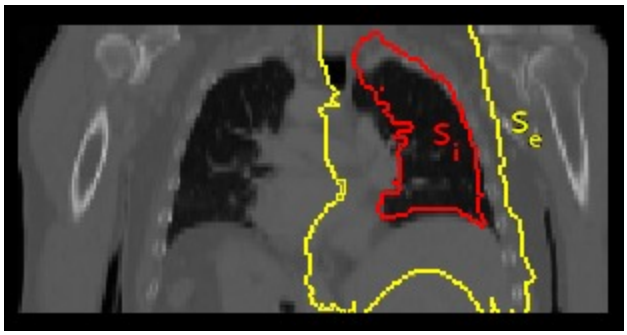

Figure 7. Coronal slice of the thorax with wrongly positioned seeds for RPS segmentation.

5. CONCLUSION

We have implemented and compared two segmentation methods based on object appearance models. The first one is an OAM which uses a thresholding on the posterior probability map for object delineation from the object's detection provided by image registration with the atlas reference system. The second one is an OCM which substitutes image registration by object search based on translations of the model over the image. By avoiding the time-costly image registration for model construction and use, and constraining object search with a small region of the image, OCM can provide a considerable speed up, being at least 600 times faster for construction and more than twice faster for use than OAM.

We have evaluated OAM and OCM for the segmentation of nine anatomical structures in MR-T1 images of the brain and CT images of the thorax. These are very challenging situations with anatomical structures in motion and absence of intensity discontinuity on their boundaries. The methods have shown to be very competitive in accuracy and we have also mentioned some ideas to improve them.

ACKNOWLEDGMENTS

The authors thank CNPq (303673/2010-9, 479070/2013-0, 131835/2013-0) and FAPESP for the finantial support.

REFERENCES

[1] Udupa, J. K., Odhner, D., Falcão, A. X., Ciesielski, K. C., Miranda, P. A. V., Vaideeswaran, P., S.Mishra, Grevera, G. J., Saboury, B., and Torigian, D. A., "Fuzzy object modeling," in [*SPIE on Medical Imaging*], **7964**, 1–10 (2011).

[2] Vos, P. C., Išgum, I., Biesbroek, J. M., Velthuis, B. K., and Viergever, M. A., "Combined pixel classification and atlas-based segmentation of the ventricular system in brain CT Images," in [*SPIE on Medical Imaging*], **8669**, 1–6 (2013).

[3] Lötjönen, J., Wolz, R., Koikkalainen, J., Thurfjell, L., Lundqvist, R., Waldemar, G., Soininen, H., and Rueckert, D., "Improved generation of probabilistic atlases for the expectation maximization classification," in [*The Eigth IEEE Intl. Symp. on Biomedical Imaging: From Nano to Macro (ISBI)*], 1839–1842 (2011).

[4] Tamez-Pea, J., González, P., Farber, J., Baum, K., Schreyer, E., and Totterman, S., "Atlas based method for the automated segmentation and quantification of knee features: Data from the osteoarthritis initiative," in [*The Eigth IEEE Intl. Symp. on Biomedical Imaging: From Nano to Macro (ISBI)*], 1484–1487 (2011).

[5] Miranda, P. A. V., Falcão, A. X., and Udupa, J. K., "*CLOUDS*: A model for synergistic image segmentation," in [*The Fifth IEEE Intl. Symp. on Biomedical Imaging: From Nano to Macro (ISBI)*], 209–212 (2008).

[6] Ciesielski, K. C., Udupa, J. K., Miranda, P. A. V., and Falcão, A. X., "Joint graph cut and relative fuzzy connectedness image segmentation algorithm," *Medical Image Analysis* **17**(8), 1046–1057 (2013).

[7] Cootes, T. F., Taylor, C. J., Cooper, D. H., and Graham, J., "Active shape models - their training and application," *Computer Vision and Image Understanding* **61**(1), 38–59 (1995).

[8] Liu, J. and Udupa, J., "Oriented active shape models," *IEEE Transactions on Medical Imaging* **28**(4), 571–584 (2009).

[9] Gao, Y. and Tannembaum, A., "Combining atlas and active contour for automatic 3D medical image segmentation," in [*The Eigth IEEE Intl. Symp. on Biomedical Imaging: From Nano to Macro (ISBI)*], 1401–1404 (2011).

[10] Grady, L., "Random walks for image segmentation," *IEEE Trans. on Medical Imaging* **28**(11), 1768–1783 (2006).

[11] Falcão, A. X. and Bergo, F. P. G., "Interactive volume segmentation with differential image foresting transforms," *IEEE Trans. on Medical Imaging* **23**(9), 1100–1108 (2004).

[12] Ciesielski, K. C. and Udupa, J. K., [*Region-based segmentation: fuzzy connectedness, graph cut, and other related algorithms - Biomedical Image Processing*], Springer-Verlag (2011). T.M. Deserno, editor.

[13] Miranda, P. A. and Falcão, A. X., "Links between image segmentation based on optimum-path forest and minimum cut in graph," *Journal of Mathematical Imaging and Vision* **35**(2), 128–142 (2009).

[14] Couprie, C., Grady, L., Najman, L., and Talbot, H., "Power watersheds: A unifying graph-based optimization framework," *IEEE Trans. Pattern Anal. Machine Intell.* **33**(7), 1384–1399 (2011).

[15] Miranda, P. A. V., Falcão, A. X., and Udupa, J. K., "Cloud Bank: A multiple clouds model and its use in mr brain image segmentation," in [*The Sixth IEEE Intl. Symp. on Biomedical Imaging: From Nano to Macro (ISBI)*], 506–509 (2009).

[16] van der Lijn, F., de Bruijne, M., Hooogendam, Y. Y., Klein, S., Hameeteman, R., and an W. J. Niessen, M. M. B. B., "Cerebellum segmentation in MRI using atlas registration and local multi-scale image descriptors," in [*The Sixth IEEE Intl. Symp. on Biomedical Imaging: From Nano to Macro (ISBI)*], 221–224 (2009).

[17] Grau, V., Mewes, A. U. J., Alcaiz, M., Kikinis, R., and Warfield, S. K., "Improved watershed transform for medical image segmentation using prior information," *IEEE Transactions on Medical Imaging* **23**(4), 447–458 (2004).

[18] Udupa, J. K., Odhner, D., Falcão, A. X., Ciesielski, K. C., Miranda, P. A. V., Matsumoto, M., Grevera, G. J., Savoury, B., and Torigian, D. A., "Automatic anatomy recognition via fuzzy object models," in [*SPIE on Medical Imaging*], **8316**, 1–8 (2012).

[19] Park, H., Bland, P. H., III, A. O. H., and Meyer, C. R., "Least biased target selection in probabilistic atlas construction," in [*Medical Image Computing and Computer-Assisted Intervention (MICCAI)*], **3750**, 419–426 (2005).

[20] Miranda, P. A. V., Falcão, A. X., and Udupa, J. K., "Cloud Models: Their construction and employment in automatic MRI segmentation of the brain," Tech. Rep. IC-10-08, Univ. of Campinas, Campinas, SP (2010).

[21] Acosta, O., Simon, A., Monge, F., Commandeur, F., Bassirou, C., Cazoulat, G., de Crevoisier, R., and Haigron, P., "Evaluation of multi-atlas-based segmentation of CT scans in prostate cancer radiotherapy," in [*The Sixth IEEE Intl. Symp. on Biomedical Imaging: From Nano to Macro (ISBI)*], 1966–1969 (2011).

[22] Chen, A., Niermann, K. J., Deeley, M. A., and Dawant, B. M., "Evaluation of multi atlas-based approaches for the segmentation of the thyroid gland in IMRT head and neck CT images," in [*SPIE on Medical Imaging*], **7962**, 1–8 (2011).

[23] Lötjönen, J., Wolz, R., and Koikkalainen, J., "Fast and robust multi-atlas segmentation of brain magnetic resonance images," *NeuroImage* **49**(3), 2352–2365 (2010).

[24] Langerak, T. R., der Heide, U. A. V., Kotte, A. N. T. J., Berendsen, F. F., and Pluim, J. P. W., "Evaluating and improving label fusion in atlas-based segmentation using the surface distance," in [*SPIE on Medical Imaging*], **7962**, 1–7 (2011).

[25] Klein, S., Staring, M., Murphy, K., Viergever, M. A., and Pluim, J. P. W., "Elastix: A toolbox for intensity based medical image registration," *IEEE Transactions on Medical Imaging* **29**(1), 196–205 (2010).

[26] Chiachia, G., Falcão, A. X., and Rocha, A., "Multiscale parameter search (msps): A deterministic approach for black-box global optimization," Tech. Rep. IC-11-15, Univ. of Campinas, Campinas, SP (2011).